

PAPER • **OPEN ACCESS**

## How to seed ergodic dynamics of interacting bosons under conditions of many-body quantum chaos

To cite this article: Lukas Pausch *et al* 2025 *Rep. Prog. Phys.* **88** 057602

View the [article online](#) for updates and enhancements.

### You may also like


- [Inherent structural descriptors via machine learning](#)  
Emanuele Telari, Antonio Tinti, Manoj Settem *et al.*
- [Metal-insulator transitions in pyrochlore oxides](#)  
Yoshinori Tokura, Yukitoshi Motome and Kentaro Ueda
- [Many-body localization in the age of classical computing](#)  
Piotr Sierant, Maciej Lewenstein, Antonello Scardicchio *et al.*

www.hidenanalytical.com  
info@hiden.co.uk

# HIDEN ANALYTICAL


## Instruments for Advanced Science

Mass spectrometers for vacuum, gas, plasma and surface science



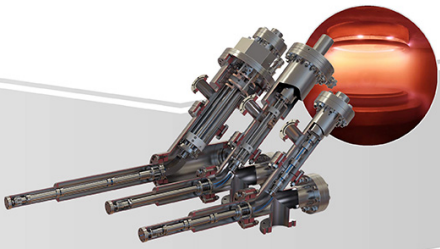
### Residual Gas Analysis

Perform RGA at UHV/XHV. Our RGA configurations include systems for UHV science applications including temperature-programmed desorption and electron/photon stimulated desorption.



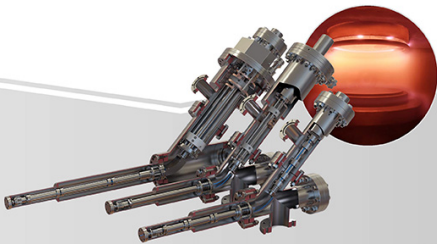
### Thin Film Surface Analysis


Conduct both static and dynamic SIMS analysis with a choice of primary ions for full chemical composition and depth profiling. Our SIMS solutions include complete workstations and bolt-on modules.



### Plasma Characterisation

Fully characterise a range of plasmas: RF, DC, ECR and pulsed plasmas, including neutrals and neutral radicals. Extend your analyses to atmospheric pressure processes using the HPR-60, with time-resolved mass/energy analysis.

 [www.HidenAnalytical.com](http://www.HidenAnalytical.com)

 [info@hiden.co.uk](mailto:info@hiden.co.uk)

# How to seed ergodic dynamics of interacting bosons under conditions of many-body quantum chaos

Lukas Pausch<sup>1,6</sup> , Edoardo G Carnio<sup>2,3</sup> , Andreas Buchleitner<sup>2,3,\*</sup> and Alberto Rodríguez<sup>4,5,\*</sup> 

<sup>1</sup> Institut de Physique Nucléaire, Atomique et de Spectroscopie, CESAM, Université de Liège, B-4000 Liège, Belgium

<sup>2</sup> Physikalisches Institut, Albert-Ludwigs-Universität Freiburg, Hermann-Herder-Straße 3, D-79104 Freiburg, Germany

<sup>3</sup> EUCOR Centre for Quantum Science and Quantum Computing, Albert-Ludwigs-Universität Freiburg, Hermann-Herder-Straße 3, D-79104 Freiburg, Germany

<sup>4</sup> Departamento de Física Fundamental, Universidad de Salamanca, E-37008 Salamanca, Spain

<sup>5</sup> Instituto Universitario de Física Fundamental y Matemáticas (IUFFyM), Universidad de Salamanca, E-37008 Salamanca, Spain

E-mail: [a.buchleitner@physik.uni-freiburg.de](mailto:a.buchleitner@physik.uni-freiburg.de) and [argon@usal.es](mailto:argon@usal.es)

Received 26 February 2025, revised 16 April 2025

Accepted for publication 25 April 2025

Published 8 May 2025

Corresponding editor: Dr Paul Mabey



## Abstract

We demonstrate how the initial state of ultracold atoms in an optical lattice controls the emergence of ergodic dynamics as the underlying spectral structure is tuned into the quantum chaotic regime. Distinct initial states' chaos threshold values in terms of tunneling as compared to interaction strength are identified, as well as dynamical signatures of the chaos transition, on the level of experimentally accessible observables and time scales.

Keywords: many-body quantum chaos, interacting bosons, ergodicity, quantum dynamics

## 1. Introduction

Spectral and dynamical properties of closed quantum systems are intimately related to each other by the spectral decomposition of the unitary time evolution operator, in terms of

the eigenenergies and -vectors of the underlying Hamiltonian [1]. The actual imprint of the uniquely determined spectral structure on the actually observed dynamics is, however, ultimately controlled by the decomposition of the specific initial state to be propagated in time, and of the measured observable, in the Hamiltonian's eigenbasis [2–4]. If the Hamiltonian features eigenstates with broadly variable localization properties in Hilbert (or phase) space, distinct initial conditions can seed very distinct dynamical behavior [5–9]. In contrast, if all eigenstates delocalize alike, to homogeneously cover the energy surface (apart from residual fluctuations—which must secure their mutual orthogonality) [10], then distinct initial states will rapidly relax into, at least on a coarse-grained level, qualitatively similar dynamical patterns, where interferences encoding the coherences between the initially populated

<sup>6</sup> Present address: German Aerospace Center, Institute of Quantum Technologies, D-89081 Ulm, Germany.

\* Authors to whom any correspondence should be addressed.



Original Content from this work may be used under the terms of the [Creative Commons Attribution 4.0 licence](https://creativecommons.org/licenses/by/4.0/). Any further distribution of this work must maintain attribution to the author(s) and the title of the work, journal citation and DOI.

eigenstates (and, thereby, the complete memory of the initial condition, which cannot be destroyed by unitary evolution, however complex this may seem) average out, on sufficiently long time scales.

As a corollary, if a Hamiltonian's eigenstate structure can be continuously tuned from broadly distributed localization properties to, in essence, uniform delocalization, by an experimentally accessible control parameter, the dynamical evolution of suitably chosen initial states must unambiguously reflect these structural changes. While such tunable structural changes and the ensuing dynamics are qualitatively reasonably well understood within the theory of quantum chaos [5], and reflect the structural metamorphoses of the underlying classical phase spaces, the latter remain largely uncharted when dealing with systems with more than two coupled degrees of freedom (DOF) [11]. The associated phase spaces may exhibit intricate structural properties not available in the low-dimensional cases [12], and the reliable mapping of these structural properties [13–15], which shape the system's eigenstates, by analysis of the induced quantum dynamics turns ever more difficult with an increasing number of DOF [16].

Within the realm of cold atom physics, this scenario is precisely realized by interacting bosons loaded into optical lattices, described, in a most elementary way, by Bose Hubbard-like Hamiltonians [17]: Each lattice site represents one degree of freedom, and the number  $L$  of lattice sites, as well as the number  $N$  of bosons per lattice site, can be controlled with high accuracy, over a broad range, such that the transition from single to many-body quantum dynamics can be continuously monitored, in phase spaces of controllable dimension [18]. Furthermore, a single parameter allows to tune the Hamiltonian's eigenstate structure, at variable  $L > 2$  and  $N$ , between the integrable and the ergodic (vulgo 'chaotic') limit [19–45]. Due to the largely unexplored phase space structure, however, it is highly non-trivial an issue which (experimentally preparable) initial states will trigger dynamics which faithfully reflect this metamorphosis, on experimentally explorable time scales.

Our present purpose therefore is to provide the first quantitative, scalable (with  $L$  and  $N$ ) analysis of how the underlying eigenstate structure of Bose–Hubbard Hamiltonians is expressed in the dynamics of experimentally accessible initial states, probed by local (i.e. interrogating only a small subset of the system's DOF) observables. More specifically, we (i) show that the dynamics of local observables—within experimentally accessible time scales—can unambiguously pinpoint the chaotic phase, in remarkable agreement with the spectral characterization, (ii) provide an analytical estimation of the onset of ergodic behavior for arbitrary Fock initial states, and (iii) illustrate how the initial state considered may affect the control parameter that drives the transition. We thus establish a scalable, quantitative benchmark of dynamical versus spectral properties of a paradigmatic quantum chaotic many-body system, opening a route towards robust control of large, strongly coupled, multi-component quantum systems with complex dynamics, an essential prerequisite for the design of quantum

computing platforms [46–48], and for the benchmarking of quantum simulators [49, 50].

The manuscript is organized as follows: In section 2, we introduce the physical model, and the family of initial states considered in our analysis. The emergence of the spectrally chaotic phase, inferred from an analysis of the localization properties of the eigenvectors, along the initial states' trajectories in energy space under variation of the Hamiltonian control parameter, is presented in section 3. The persistence of the chaotic domain as the thermodynamic limit (TL) is approached, and the definition of the control parameter driving the chaos transition are discussed in section 4, where we give an analytical estimate for the critical parameter value which defines the onset of chaos. In section 5, we finally benchmark the many-body dynamics seeded by the selected initial states against the underlying spectral and eigenvector structure, by studying the dynamics of experimentally accessible local observables. A summary of our findings is finally presented in section 6.

## 2. Physical model and initial states

We study the one-dimensional, particle-number conserving Bose–Hubbard Hamiltonian (BHH) [51–54] of  $N$  bosons on  $L$  sites,

$$H = -J \sum_{j=1}^{L-1} (a_j^\dagger a_{j+1} + a_{j+1}^\dagger a_j) + \frac{U}{2} \sum_{j=1}^L a_j^\dagger a_j^\dagger a_j a_j, \\ \equiv -J h_{\text{tun}} + U h_{\text{int}}, \quad (1)$$

where  $h_{\text{tun}}$  and  $h_{\text{int}}$  denote, respectively, the dimensionless tunneling and interaction terms,  $a_j^{(\dagger)}$  are creation and annihilation operators, associated with Wannier orbitals localized at each lattice site, and hard-wall boundary conditions (HWBCs) are employed, as in typical experimental realizations with ultracold atoms in optical lattices.

The Hamiltonian exhibits reflection symmetry about the center of the chain, i.e.  $[H, \Pi] = 0$ , where  $\Pi$  is the reflection operator. The Hilbert space of total dimension  $\mathcal{D}$  thus decomposes into the direct sum

$$\mathcal{H} = \mathcal{H}^+ \oplus \mathcal{H}^- \quad (2)$$

of the symmetric (even parity) and the antisymmetric (odd parity) subspace,  $\mathcal{H}^+$  and  $\mathcal{H}^-$  (of dimensions  $\mathcal{D}^+$  and  $\mathcal{D}^-$ ), respectively, which are invariant under the dynamics induced by  $H$ .

In the limit of vanishing tunneling strength,  $J = 0$ , as well as in the non-interacting limit,  $U = 0$ , the BHH is integrable, and one finds as many independent and mutually commuting observables as the model's DOF, here given by the number  $L$  of sites [55]. The eigenstates in those limits are thus Fock states uniquely identified by  $L$  quantum numbers. For instance, the

eigenstates in  $\mathcal{H}^+$  for  $J = 0$  are

$$|n^+\rangle = \frac{1}{\sqrt{2(1 + \delta_{n,\Pi n})}} (\mathbb{1} + \Pi) |n\rangle, \quad (3)$$

with  $|n\rangle \equiv |n_1, \dots, n_L\rangle$ , and  $n_j$  the eigenvalues of the on-site number operators  $\hat{n}_j = a_j^\dagger a_j$ .

When  $J \neq 0$  and  $U \neq 0$ , the interplay of tunneling and interaction renders the BHH non-integrable and an ergodic phase emerges as a function of  $J$  and  $U$ , which can be identified from spectral and eigenvector features [20, 23, 27, 31–33]. In experiments with ultracold atoms, its existence is probed by analyzing the dynamics of non-equilibrium initial configurations, which are typically Fock states in the on-site basis [41, 56–68]. Most common initial states include (i) the homogeneous density configuration [41, 56–63], (ii) staggered density distributions [64–66], and (iii) atomic clouds initially loaded into a strictly confined portion of the lattice, beyond which they can subsequently expand [67, 68].

We here analyze the signature of the chaotic phase in the eigenstate decomposition and in the time evolution of exemplary Fock initial states of the above types, defined as:

- (i) The *homogeneous* density Fock state

$$|\psi_h\rangle \equiv |n, \dots, n\rangle, \quad (4)$$

for integer  $n = N/L$ . This configuration carries an enhanced weight of the system's ground state within the Mott insulator phase [69], and becomes the exact ground state in the limit  $J/U \rightarrow 0$ .

- (ii) The *staggered* configuration  $|\psi_s\rangle$  that at fixed density lies deepest in the spectrum bulk, (i.e. whose energy corresponds best to the arithmetic mean of the Hamiltonian's spectrum), and hence may exhibit maximal sensitivity to the emergence of spectral chaos. For  $n = 1$ , the corresponding Fock state has  $\lfloor (N-2)/3 \rfloor$  sites occupied by 3 particles each, and 2 sites hosting 1 or 2 particles, to ensure the desired  $N$ , e.g.  $|\psi_s\rangle = |0203003020\rangle$  for  $N = L = 10$  [70]. Note that, at given density  $n$ , the staggered state's energy traces that of the maximally mixed (or 'infinite temperature') state  $\rho_{\text{MM}} = \mathbb{1}/\mathcal{D}$  (see appendix A), though the former state is pure, and thus exhibits coherences, what the latter does not.
- (iii) The *localized* initial state  $|\psi_\ell\rangle$ , where all  $N$  particles are localized within  $\ell$  sites around the center of the lattice (we will here consider  $\ell = 3$  in all subsequent calculations), each with  $\lfloor N/\ell \rfloor$  or  $\lceil N/\ell \rceil$  particles, for given  $n$ .

### 3. Parametric evolution of initial state energies

Let us now first analyze the spectral and eigenvector structure of the BHH, and its parametric evolution with variable  $J$  and  $U$ , which we later want to certify through the observation of suitably chosen dynamical variables. For this latter purpose,

we additionally need to consider which eigenstates are significantly populated by the choice of either one of the initial states (i–iii) above, as well as the parameter dependence of this decomposition. Distinct decompositions will define distinct passages of the given initial states across the parameter space's chaotic domain, and thus lead to potentially different experimental records—triggering distinct interpretations.

We probe eigenvector ergodicity (in Fock space) using the finite-size generalized fractal dimension  $\tilde{D}_1$ ,

$$\tilde{D}_1 = -\frac{1}{\log \mathcal{D}} \sum_{\alpha} |\psi_{\alpha}|^2 \log |\psi_{\alpha}|^2 \in [0, 1], \quad (5)$$

where  $\psi_{\alpha}$  is the amplitude of the state  $|\psi\rangle$  on the basis state  $|\alpha\rangle$  (e.g. the basis given in equation (3)). As we demonstrated in [31–33, 55], the chaotic region correlates with large  $\tilde{D}_1$ , converging towards unity in the limit  $\mathcal{D} \rightarrow \infty$  [which corresponds to fully extended (ergodic) states in Hilbert space], and, most significantly, with strongly suppressed eigenstate-to-eigenstate fluctuations of  $\tilde{D}_1$ .

Figure 1(a) shows the chaotic phase for  $N = L = 10$ , exposed by the suppressed variance of  $\tilde{D}_1$  over close-in-energy eigenstates, in terms of the relative tunneling strength

$$\gamma \equiv J/U, \quad (6)$$

and of the scaled energy [31]

$$\varepsilon = \frac{E - E_{\min}}{E_{\max} - E_{\min}}, \quad (7)$$

where  $E_{\min(\max)}$  denotes the minimum (maximum) eigenenergy for each  $J/U$ . We also show the initial states' (i–iii) trajectories in energy space under variation of  $\gamma$ , as determined by

$$E_h \equiv \langle \psi_h | H | \psi_h \rangle = \frac{UN}{2} (n - 1), \quad (8)$$

$$E_s \equiv \langle \psi_s | H | \psi_s \rangle = U(N - 2), \quad (9)$$

$$E_\ell \equiv \langle \psi_\ell | H | \psi_\ell \rangle = \frac{U}{2\ell} (N - r_{N/\ell}) (N + r_{N/\ell} - \ell), \quad (10)$$

where  $r_{N/\ell} \equiv (N \bmod \ell) \in [0, \ell - 1]$ , and, by choice,  $E_s$  approximates the energy

$$\begin{aligned} E_{\text{MM}} &\equiv \text{Tr}(H\rho_{\text{MM}}) = U \frac{N(N-1)}{L+1} \\ &= U [nN - n(n+1) + O(N^{-1})] \end{aligned} \quad (11)$$

of the maximally mixed state  $\rho_{\text{MM}}$ , with  $n = 1$  (see appendix A for the derivation of  $E_{\text{MM}}$ ).

As can be observed in figure 1(a), the Fock initial states' trajectories do not remain at a constant level of the scaled energy. Instead,  $\varepsilon$  varies strongly with  $\gamma$ , along each trajectory, and the chaotic phase is entered at different points by the different initial states' trajectories, before they all converge into the



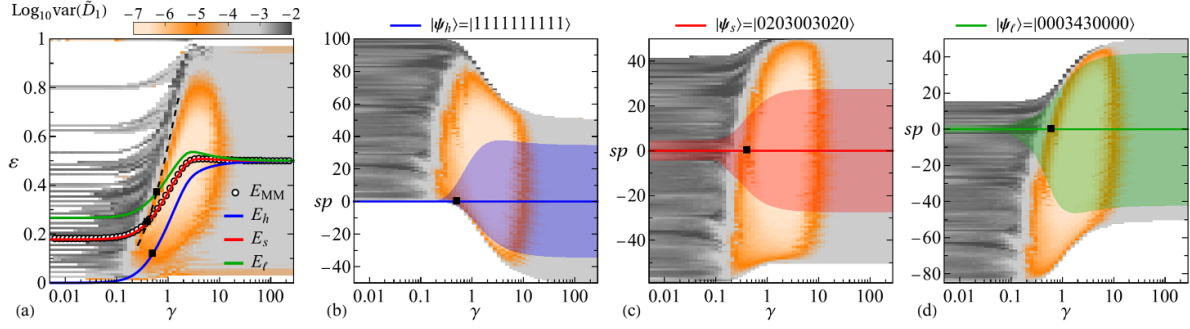


**Figure 1.** Perspectives of the chaotic phase for  $L = N = 10$  (HWBC, subspace  $\mathcal{H}^+$ ,  $\mathcal{D}^+ = 46252$ ) revealed by  $\text{var}(\tilde{D}_1)$  as a function of  $\gamma = J/U$  and (a) the scaled energy  $\varepsilon = (E - E_{\min})/(E_{\max} - E_{\min})$  or (b)–(d) the spectrum percentage ( $sp$ ) measured from the reference energy of the indicated Fock states. For each  $J/U$  value, the eigenstates are sorted into 100 sets that (a) correspond to intervals of constant width in  $\varepsilon$  or (b)–(d) contain the same number of states (i.e. same spectrum percentage), and  $\text{var}(\tilde{D}_1)$  is evaluated for each set. Solid lines in (a) show the energy trajectories of the selected Fock states (equations (8)–(10)), while symbols correspond to the maximally mixed state (equation (11)). Shaded regions in (b)–(d) mark the energy width  $\pm\sigma$  (equation (12)) of each Fock state in terms of  $sp$ . Black squares indicate the threshold values  $\gamma^c$  from equation (19) ( $|\psi_h\rangle$ ) and equation (20) ( $|\psi_s\rangle$ ,  $|\psi_l\rangle$ ), which gives the dashed trajectory in (a).

same limiting value  $\varepsilon = 0.5$ , for  $\gamma \rightarrow \infty$  [71]. Hence, chaos emerges differently along the energy trajectory of each Fock initial state, and, consequently, in the associated dynamical behavior (as we will confirm further down).

Panels (b)–(d) in figure 1 present the chaotic phase, in terms of  $\text{var}(\tilde{D}_1)$ , as a function of  $\gamma$ , and of the percentage of the spectrum that lies above and below the given initial state's energy, for  $N = L = 10$  and  $\ell = 3$ . Once the region of uniformly delocalized eigenstates, characterized by a strongly suppressed variance  $\text{var}(\tilde{D}_1)$  of the generalized fractal dimension emerges, it practically extends over the entire spectrum.

Also shown is the evolution of the energy width  $\pm\sigma$  of each Fock initial state, in terms of the spectral percentage, given by

$$\sigma_{|n\rangle}^2 \equiv \langle H^2 \rangle_{|n\rangle} - \langle H \rangle_{|n\rangle}^2 = J^2 \left( 2N - n_1 - n_L + 2 \sum_{j=1}^{L-1} n_j n_{j+1} \right), \quad (12)$$

for  $|n\rangle = |\psi_{h,s,\ell}\rangle$ . This energy scale quantifies the width of the local density of states (LDOS) of  $H$  with respect to  $|\psi_{h,s,\ell}\rangle$ , and hence of the spectral region where eigenstates of  $H$  noticeably contribute to  $|\psi_{h,s,\ell}\rangle$ .

The plots thus illustrate how the chaotic phase unfolds from the perspective of the different initial states  $|\psi_h\rangle$  (b),  $|\psi_s\rangle$  (c), and  $|\psi_l\rangle$  (d): As  $\gamma$  is increased from the strongly interacting limit, the entrance of each Fock state into the chaotic domain correlates with a pronounced increase of  $\sigma$  in terms of the spectral percentage, consistent with the emerging ergodic structure of chaotic eigenstates in Fock space. The number of eigenstates that contribute dominantly to each Fock initial state reaches its maximum around the center of the chaotic phase, and barely changes as the non-interacting limit is approached. In the  $\gamma$  range where each initial state picks up significant contributions from ergodic eigenstates, the dynamical manifestations of chaos must become observable.

#### 4. Persistence of ergodicity in the TL

In the previous section, we analyzed the passage of the initial state trajectories across energy space, under variation of  $\gamma$ , and at fixed particle number  $N$  and density  $n$ . Since quantum chaos and also random matrix theory explore quantum signatures [72] of classical mechanics and thermodynamics, it is important to clarify how the essential features identified in such analysis evolve with the system size, and in particular in the TL, i.e. for  $N \rightarrow \infty$ , fixed  $n$  [73].

To monitor this evolution with the initial states (i–iii) as reference, Figure 2 shows the mean and the variance of  $\tilde{D}_1$  over the  $\gtrsim 100$  eigenstates closest in energy to (a)  $E_h$ , (b)  $E_s$ , and (c)  $E_l$  [and therefore certainly within their respective energy widths  $\sigma$  as indicated in figures 1(b)–(d)], as functions of  $\gamma$ , and for  $N \in [7, 13]$  and  $n = 1$ . That number of eigenstates is small enough to probe the properties of the spectrum only locally and large enough to ensure good statistics for  $\langle \tilde{D}_1 \rangle$  and  $\text{var}(\tilde{D}_1)$ . In all three cases, the ergodic phase is revealed by plateaux of maximal  $\langle \tilde{D}_1 \rangle$  (converging to unity, in the TL), correlating with minimal  $\text{var}(\tilde{D}_1)$  (converging to 0, in the TL), which are both well described by the corresponding values obtained from the Gaussian orthogonal ensemble (GOE) of random matrices [31–33]. As the system size is increased, the ergodic phase in the spectral vicinity of the homogeneous  $|\psi_h\rangle$  [panel (a)] and of the staggered density state  $|\psi_s\rangle$  [panel (b)] is getting ever more clearly exposed, within a well-defined range of  $\gamma$  values. In contrast, the emergence of chaos in the spectral vicinity of the localized density state  $|\psi_l\rangle$  [panel (c)] systematically shifts to larger  $\gamma$  with increasing system size [note the consistent displacement of the  $\langle \tilde{D}_1 \rangle$  curves and of the minimum in  $\text{var}(\tilde{D}_1)$ ]. Only when the tunneling strength is scaled as

$$\eta \equiv J/UN \quad (13)$$

(panel (d)) is this shift removed and the appearance of the chaotic region eventually becomes system-size independent.

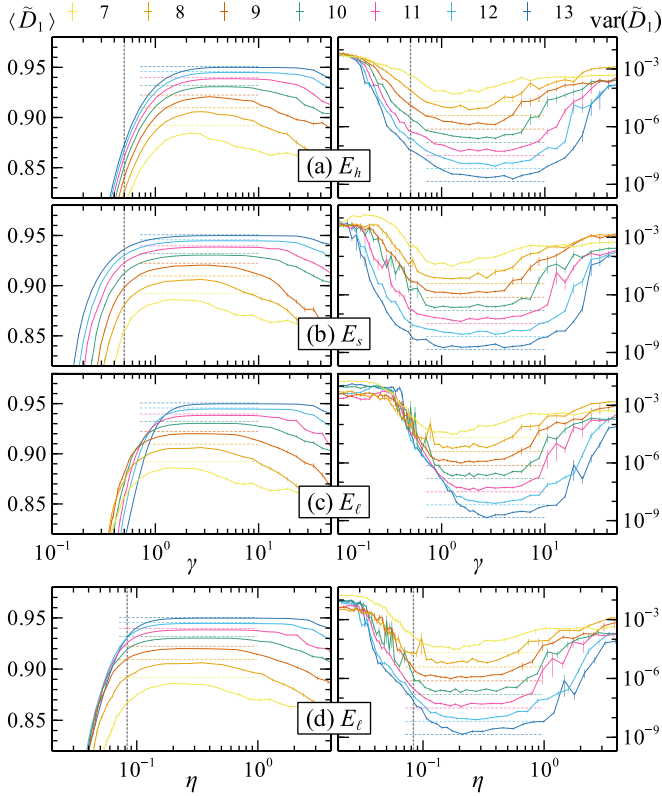


**Figure 2.** Dependence on  $\gamma = J/U$  (top three rows) and on  $\eta = J/UN$  (bottom row) of  $\langle \tilde{D}_1 \rangle$  (left column) and of  $\text{var}(\tilde{D}_1)$  (right column) calculated from  $\gtrsim 100$  eigenstates (subspace  $\mathcal{H}^+$ ) closest in energy to (a) the homogeneous density state  $|\psi_h\rangle$ , (b) the staggered density state  $|\psi_s\rangle$ , and (c), (d) the localized density state  $|\psi_\ell\rangle$  for varying values of  $N = L \in [7, 13]$  with  $\mathcal{D}^+ \in [868, 2600612]$ . Horizontal dashed lines indicate GOE predictions for the corresponding Hilbert space size. Vertical dashed lines mark the threshold values  $\gamma^c$  for  $N \rightarrow \infty$  from equations (19) and (20), respectively for (a) and (b), and  $\eta^c$  from equation (21) for (d).

While this may appear intuitive, since increasing  $N$  at fixed  $n$  and  $\ell$  increases the effective interaction strength for  $|\psi_\ell\rangle$ , such that also  $\gamma$  needs to be increased to compensate this effect, we will now make this argument more quantitative, by closer inspection of the associated scaling properties of the spectrum. This will allow us to extract the critical values of  $\gamma$  and  $\eta$ , respectively, at which the chaos transition occurs for the different initial states.

In general, for a chaotic spectral and eigenstate structure to persist, the tunneling and the interaction terms in  $H$ —which represent incompatible integrals of motion—need to balance each other: If either of them became progressively dominant as the boson number is increased, the system would be drawn into the corresponding integrable phase. It is therefore instructive to consider the scaling behavior of the tunneling and of the interaction contribution to  $H$ : The spectral width,

$$\Delta E \equiv E_{\max} - E_{\min}, \quad (14)$$

of the tunneling term reads  $\Delta E_{\text{tun}} = 4JN$  and, hence, scales linearly with  $N$ . On the other hand, at integer density  $n$ , the

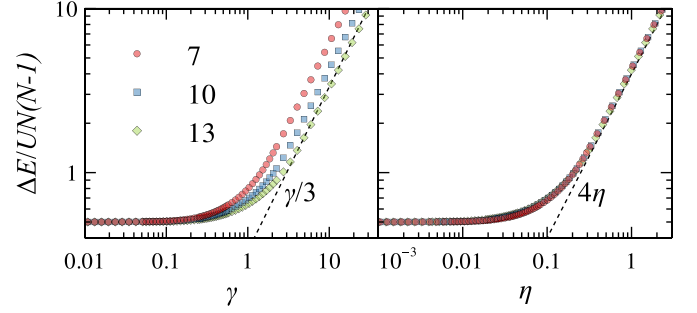


**Figure 3.** Spectral width  $\Delta E = E_{\max} - E_{\min}$  of  $H$  scaled by  $UN(N-1)$  versus  $\gamma = J/U$  (left) and  $\eta = J/UN$  (right), for  $N = L \in [7, 13]$  as indicated. Dashed lines denote the exact linear dependence of the scaled spectral width in the limits  $\gamma \rightarrow \infty$  (for  $N = 13$ ) and  $\eta \rightarrow \infty$  (for  $N \rightarrow \infty$ ).

spectral width  $\Delta E_{\text{int}} = UN(N-n)/2$  of the interaction term scales quadratically with  $N$ . The interaction term will therefore induce a shift  $\propto N^2$  of some eigenenergies when the TL is approached at constant particle density.

This is demonstrated in figure 3, for  $n = 1$ , via the dependence of the scaled spectral width  $\Delta E/UN(N-1)$  on  $\gamma$ ,  $\eta$ , and  $N$ . In the strong interaction regime ( $\gamma, \eta \rightarrow 0$ ), the scaled spectral width converges to  $1/2$ , while it approaches the asymptotes  $4\gamma/(N-1)$  and  $4\eta$  in the tunneling-dominated regime, i.e. for  $\gamma \gg 1$  and  $\eta \gg 1$  (provided  $N \gg 1$ , in the latter case), respectively. Notably, the scaled spectral width becomes system-size independent as a function of  $\eta$ , and the crossover between both regimes can be located in terms of the rescaled tunneling strength at  $\eta_* \simeq 1/8$ . Since, for  $\eta < \eta_*$ , there is a subset of eigenenergies which scale, at fixed  $n$  and  $\gamma$ , quadratically with  $N$ , the interaction term will progressively dominate their character as  $N$  increases, and they must exit the chaotic phase, in the TL.

The energy expectation values (equations (8)–(10)) of the Fock initial states (i–iii) are, by construction, entirely determined by the interaction term in (1), and these scale, at fixed  $n$ , as  $E_{h,s} \sim N$  and  $E_\ell \sim N^2$ . This different scaling reflects the initial states' structure, which for  $|\psi_{h,s}\rangle$  explores the entire lattice (which grows with  $N$ , since  $n$  is kept constant in the TL), while for  $|\psi_\ell\rangle$  concentrates ever more particles on  $\ell$  sites, thus activating the inter-particle interaction term. Consequently, at fixed  $\gamma$  and  $n$ ,  $|\psi_\ell\rangle$  will remain interaction-dominated at sufficiently large  $N$ , and hence exit the chaotic domain, as visible in figure 2(c). Only when this concentration effect is compensated by rescaling  $U$  with  $N$  does the extent of the ergodic phase for  $|\psi_\ell\rangle$  remain well-defined in the TL, in terms of  $\eta$  (see figure 2(d)). This is in line with studies of the semiclassical limit of the BHH [27, 74–76], where the relevant system parameters determining the emergence of chaos are  $\eta$  and  $E/UN^2$ , and the limit  $n \rightarrow \infty$  is performed at constant  $L$ —reminiscent of our present scenario for  $|\psi_\ell\rangle$ , locally on the  $\ell$  initially occupied sites.

Given the above scaling arguments, for chaos to prevail in the TL for given Hamiltonian parameters  $J$  and  $U$ , this limit needs to be approached at constant energy density  $\omega \equiv \langle H \rangle / N$ .

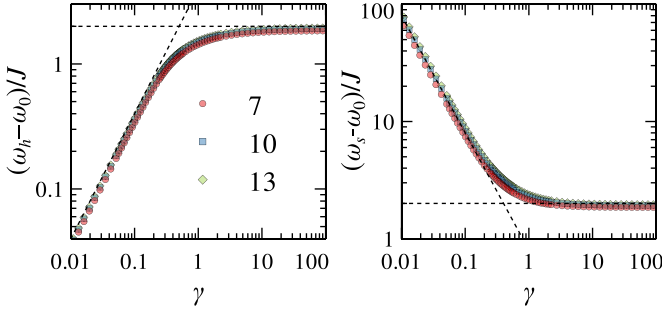


**Figure 4.** Energy density excess  $(\omega - \omega_0)/J$  as a function of  $\gamma = J/U$  for  $|\psi_h\rangle$  (left) and  $|\psi_s\rangle$  (right). Dashed lines show the asymptotic tendencies given in equation (18) (with  $N = 10$  for  $|\psi_s\rangle$ ).

At well-defined  $\omega$ , however, also an appropriate choice of  $\gamma$  is required to balance the contributions of the tunneling and interaction terms in  $H$ .

For a given  $\omega$ , one may obtain a rough estimate of the  $\gamma$  value at which the chaotic domain appears by analyzing the behavior of  $(\omega - \omega_0)/J$  as a function of  $\gamma$ , where  $\omega_0$  corresponds to the Hamiltonian's ground state's energy density. For Fock states,

$$\frac{\omega}{J} = \frac{1}{\gamma} \frac{\langle h_{\text{int}} \rangle}{N}, \quad (15)$$

while, at integer density,

$$\frac{\omega_0}{J} = \frac{n-1}{2\gamma} - 2(n+1)\gamma + O(\gamma^3), \quad \gamma \rightarrow 0, \quad (16)$$

$$\frac{\omega_0}{J} = -2 + O(1/\gamma), \quad \gamma \rightarrow \infty, \quad (17)$$

as follows from standard perturbation theory. Therefore, asymptotically, one has

$$\frac{\omega - \omega_0}{J} \underset{\gamma \rightarrow 0}{=} \frac{1}{\gamma} \left( \frac{\langle h_{\text{int}} \rangle}{N} - \frac{n-1}{2} \right) + 2(n+1)\gamma, \quad (18a)$$

$$\frac{\omega - \omega_0}{J} \underset{\gamma \rightarrow \infty}{=} 2, \quad (18b)$$

where two terms are kept in the limit  $\gamma \rightarrow 0$  to account for the case where  $\langle h_{\text{int}} \rangle/N = (n-1)/2$ , as it precisely happens for  $|\psi_h\rangle$ . The above two limiting behaviors govern the evolution of the energy density excess  $(\omega - \omega_0)/J$  in terms of  $\gamma$ , as demonstrated in figure 4 for  $|\psi_h\rangle$  and  $|\psi_s\rangle$ . The crossing point of both asymptotic tendencies may be used as an estimate of the threshold value  $\gamma^c$  at which the tunneling term starts taming the interaction contribution, and hence of the region where one expects chaos to emerge. According to equations (18), for the homogeneous state, which happens to be the Fock state with the lowest possible energy density,  $\omega/J = (n-1)/2\gamma$ , the crossing point reads

$$\gamma_h^c = \frac{1}{n+1}, \quad (19)$$

and, for a Fock state with higher energy density,

$$\gamma^c = \frac{1}{2} \left( \frac{\langle h_{\text{int}} \rangle}{N} - \frac{n-1}{2} \right). \quad (20)$$

For  $|\psi_h\rangle$  and  $|\psi_s\rangle$  at unit density, one has  $\gamma_h^c = 1/2$ , and  $\gamma_s^c = (1 - 2/N)/2 \approx 1/2$  for large  $N$ , which, as indicated in figures 2(a)–(b) and figures 1(b)–(c), describe qualitatively well the threshold of the region with ergodic eigenstates, and the entrance of these Fock initial states into the chaotic domain. The estimate (20) may also be applied to the case where  $\langle h_{\text{int}} \rangle \sim N^2$ . In this case, one obtains, at constant density and for large  $N$ ,

$$\eta^c \simeq \frac{1}{2} \frac{\langle h_{\text{int}} \rangle}{N^2}, \quad (21)$$

which for  $|\psi_\ell\rangle$  captures fairly well the appearance of the chaotic regime as the TL is approached, as observed in figure 2(d). Furthermore, the relation (20) between the dimensionless energy density  $\langle h_{\text{int}} \rangle/N$  and the threshold value  $\gamma^c$ , when visualized in terms of the scaled energy  $\varepsilon$  for fixed  $N$ , describes correctly the tilt of the chaotic phase towards higher relative tunneling strengths for larger scaled energies, as indicated in figure 1(a).

## 5. Dynamical behavior of experimentally accessible local observables

Our above analysis of the spectral and eigenvector properties of  $H$  led to an estimate for the chaos threshold of different Fock states  $|\psi_{h,s,\ell}\rangle$ , and the scaling of the states' energy densities when approaching the TL allowed us to conclude whether such threshold correlates with well-defined threshold values  $\gamma^c$  or  $\eta^c$ , for varying system sizes.

Let us now investigate how this spectral picture translates into dynamical features. For this purpose, we calculate the time evolution of the initial states  $|\psi_h\rangle$ ,  $|\psi_s\rangle$ , and  $|\psi_\ell\rangle$ , for increasing system size, at constant density  $n = 1$ , up to a maximum of 200 tunneling times,  $\tau \equiv tJ/\hbar < 200$ , chosen to lie within time scales experimentally accessible with ultracold bosons, as those probed in references [59, 63]. The dynamical evolution is numerically generated by means of an expansion of the unitary time evolution operator in terms of Chebyshev polynomials, which permits to efficiently simulate the dynamics in large Hilbert spaces (see appendix B for technical details). For simplicity, we will restrict ourselves to observables that can be easily reconstructed from uncorrelated measurements of single-site densities, and which are thus within reach for state-of-the-art experiments.

### 5.1. Homogeneous Fock state

We start out with the homogeneous initial configuration,  $|\psi_h\rangle$ . The top panels of figures 5(a) and (b) show, respectively, the time evolution of the on-site density expectation value  $\langle n_c(\tau) \rangle$ , and of the corresponding fluctuations  $\Delta n_c^2(\tau) \equiv \langle [n_c(\tau) - \langle n_c(\tau) \rangle]^2 \rangle$ , measured at a central site with index

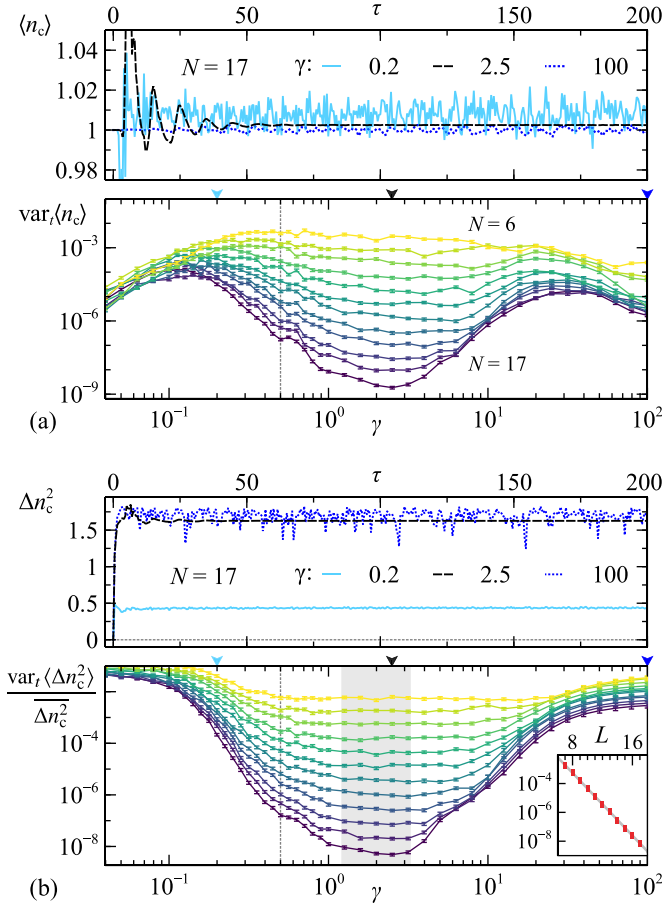


**Figure 5.** Dynamical features of (a) on-site density expectation values  $\langle n_c(\tau) \rangle$  and (b) the fluctuations  $\Delta n_c^2(\tau)$  on a central site (as explained in the main text), for the initially homogeneous configuration  $|\psi_h\rangle$ . The upper panel in each subfigure shows the time evolution for  $N=17$  and three values of  $\gamma$  as indicated (marked in the lower panels by correspondingly colored arrowheads). Each lower panel displays the (relative) time variance of the corresponding signal as a function of  $\gamma$  for  $N=L \in [6, 17]$  (from top to bottom). The vertical dashed lines indicate  $\gamma_h^c = 1/2$  (equation (19)). The inset in (b) shows the relative time variance averaged in the shaded area versus  $L$ , where the solid line is the best fit  $12.15e^{-1.25L}$ .

$[L/2]$ , i.e. taken to be the closest site (from the left) to the lattice center. This choice permits to treat even and odd system sizes on an equal footing. Given the initially homogeneous density, no net mass transport in time across the system can be expected in the TL, and, hence, on-site densities for finite  $L$  should merely exhibit small variations around the value  $n=1$ , induced by the presence of hard-wall boundaries, as observed in figure 5(a) for  $N=17$  and three representative values of  $\gamma$ . For  $\gamma=2.5$ , which is deep in the chaotic regime, according to our above spectral analysis, initial oscillations in  $\langle n_c(\tau) \rangle$  fade out on the time scale of  $\tau \approx 50$  tunneling times, and the central site then equilibrates, settling at a sharp value of  $\langle n_c \rangle$  [77]. In contrast, temporal fluctuations persist throughout the entire time window for the other two  $\gamma$  values, representing the

**Table 1.** Initial Fock states at unit density describing staggered density configurations whose energy corresponds best to the arithmetic average of the Hamiltonian's spectrum (cf equations (9) and (11)).

$L$	$ \psi_s\rangle$
11	$ 01030303010\rangle$
13	$ 0200303030020\rangle$
14	$ 01030300303010\rangle$
16	$ 0200303003030020\rangle$
17	$ 01003030303030010\rangle$

interaction-dominated and tunneling-dominated regimes. An analogous behavior is found for the on-site number variance  $\Delta n_c^2(\tau)$  in figure 5(b), which again settles at a sharp value, for  $\gamma=2.5$  and  $\tau \geq 50$ , while outside the chaotic domain also this two-particle observable (sensitive to two-particle interference contributions [8]) exhibits persistent fluctuations.

We quantify the time fluctuations of the expectation value  $\langle O(\tau) \rangle$  of a given observable  $O$  by its temporal variance in the interval  $\tau \in [\tau_1, \tau_f]$ ,

$$\text{var}_t \langle O \rangle = \frac{1}{\tau_f - \tau_1} \int_{\tau_1}^{\tau_f} d\tau \left( \langle O(\tau) \rangle - \overline{\langle O(\tau) \rangle} \right)^2, \quad (22)$$

where the overline denotes the time average within the same time interval. The lower panels in figures 5(a) and (b) show, respectively, the temporal variance for  $\tau \in [100, 200]$  of the signals  $\langle n_c(\tau) \rangle$  and  $\Delta n_c^2(\tau)$  (the relative variance in this latter case, i.e. scaled by  $\Delta n_c^2(\tau)^2$ ), as functions of  $\gamma$ , for varying system size. For the local one- and two-particle observables considered, a distinctive regime of markedly suppressed temporal fluctuations emerges in the range  $0.2 \lesssim \gamma \lesssim 20$  for all system sizes, which correlates unambiguously with the chaotic phase identified in the preceding spectral and eigenvector analysis (cf figures 1(b) and 2(a)). The analytically obtained value  $\gamma_h^c = 1/2$  also captures correctly the threshold of the region with minimal temporal fluctuations, which are ever reducing for increasing system size. As demonstrated in the inset to figure 5(b), these fluctuations decrease exponentially with  $L$  (i.e. with the number of DOF of the system [55]), in accordance with the emergence of an ergodic dynamical regime [78, 79].

These observations then confirm  $\gamma$  as the parameter that controls the dynamical appearance of the chaotic phase for  $|\psi_h\rangle$ , as deduced from the energy scaling in the previous section.

## 5.2. Staggered density configuration

Let us now study the dynamics of initial Fock states  $|\psi_s\rangle$  corresponding to staggered density configurations. As discussed in section 2, these states, given in table 1 for different  $L$ , lie deep in the spectrum bulk, their energies being closest to the arithmetic average of the Hamiltonian's spectrum (cf equations (9) and (11)).



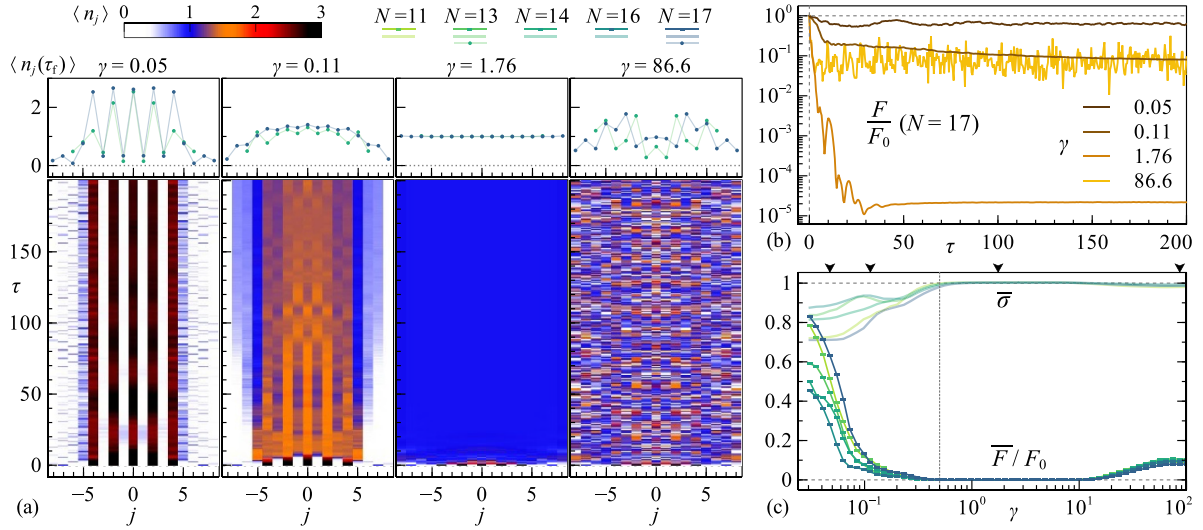


**Figure 6.** Dynamical observables for the initially staggered density configurations given in table 1. Density plots in (a) show the evolution of on-site density expectation values  $\langle n_j(\tau) \rangle$  with tunneling time  $\tau$  for  $N = 17$  and the four values of  $\gamma$  indicated [also marked by arrowheads in panel (c)], and are topped by the spatial density profiles at the final evolution time  $\tau_f = 200$ . The time evolution of the density mean square deviation  $F(\tau)$  (equation (24), scaled by  $F_0 \equiv F(\tau = 0)$ ) corresponding to the density plots is displayed in panel (b). The time-averaged value of the density profile width (equation (23)),  $\bar{\sigma}$ , and of the density mean square deviation,  $\bar{F}$ , in the interval  $\tau \in [100, 200]$  are shown as functions of  $\gamma$  for varying system sizes (color coded) in panel (c). The vertical dotted line in (c) marks the threshold value  $\gamma_s^c = 1/2$  from equation (20) for  $N \rightarrow \infty$ .

In this case, given the non-homogeneous nature of the initial state, useful information can be gathered by monitoring the evolution of the spatial density profile (defined by the on-site density expectation values  $\langle n_j(\tau) \rangle$ ), with an example displayed for  $N = 17$  and four representative  $\gamma$  values in figure 6(a). For  $\gamma = 0.05$ , the large value of the interaction energy induces self-trapping, and the bosons remain localized on initially multiply occupied sites, flanked by oscillations of two single particles at the lattice ends. Traces of the initial condition thus remain well visible at the final time  $\tau_f = 200$  (see top panels in figure 6(a)). Increasing the relative tunneling strength, for  $\gamma = 0.11$ , we observe a progressive melting of the staggered pattern and the formation of a density cloud that falls off towards the edges. Deep in the chaotic phase as demarcated in our spectral analysis, for  $\gamma = 1.76$ , the density profile homogenizes very quickly, and after  $\approx 10$  tunneling times the density distribution remains equilibrated in time, without any manifestation of the many-particle dynamics' coherent nature. When approaching the non-interacting limit, for  $\gamma = 86.6$ , the entire evolution is strongly imprinted by interference effects, and the spatial density distribution, although arguably more homogeneous than initially, exhibits persistent temporal fluctuations.

The emergence of many-body quantum chaos entails a fast temporal growth of the entanglement among multiple DOF (here associated with the individual lattice sites) of the system. The reduced density matrices  $\rho_{\text{red}}$  of small subsystems (i.e. involving reduced DOF subsets) will thus quickly develop a strong mixedness, and, correspondingly, the expectation values of local observables (living on a subset of lattice sites), which would be entirely determined by a state of the form  $\rho_{\text{red}}$ ,

dephase rapidly in time and converge to a steady state value, as reflected by the single-particle expectation values  $\langle n_j(\tau) \rangle$  for  $\gamma = 1.76$  (and the total absence of interference-induced patterns) in figure 6(a).

To identify dynamically the chaotic phase from the behavior of the density profile, we characterize the spatial width of the atomic cloud by

$$\sigma(\tau) = \frac{1}{\sigma_u} \left[ \sum_{j=1}^L \frac{\langle n_j(\tau) \rangle}{N} \left( j - \frac{L+1}{2} \right)^2 \right]^{1/2}, \quad (23)$$

which gives the standard deviation of the discrete distribution  $\langle n_j(\tau) \rangle/N$ ,  $j = 1, \dots, L$ , normalized with respect to the value for a discrete uniform distribution,  $\sigma_u = \sqrt{(L^2 - 1)/12}$ . We further quantify the cloud's homogeneity by the mean square deviation of the on-site density values from  $n$ ,

$$F(\tau) = \frac{1}{L} \sum_{j=1}^L [\langle n_j(\tau) \rangle - n]^2, \quad (24)$$

which vanishes for a uniform density distribution.

The evolution of  $F(\tau)$  shown in figure 6(b) for  $N = 17$  encodes the time development of the density profiles of figure 6(a): While deviations from homogeneity are notable for low and high relative tunneling strengths,  $F(\tau)$  drops quickly by several orders of magnitude for  $\gamma = 1.76$ .

The time-averaged values, over the interval  $\tau \in [100, 200]$ , of the figures of merit (23) and (24), as functions of  $\gamma$ , and for varying system size, are displayed in figure 6(c). There,

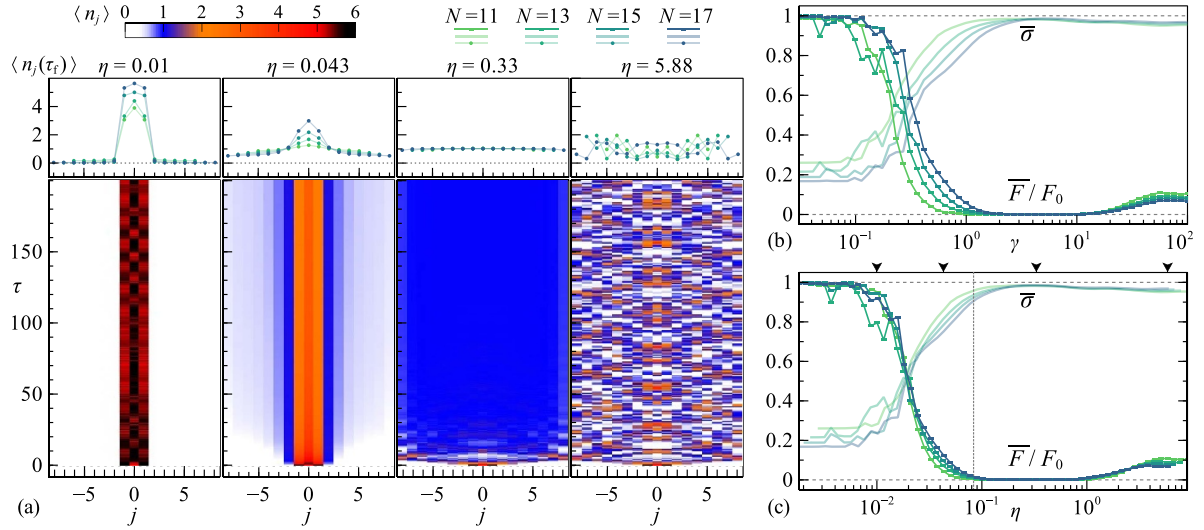


**Figure 7.** Dynamical observables for initially localized Fock states  $|\psi_\ell\rangle$  with  $\ell = 3$  central sites populated as  $\{|434\rangle, |454\rangle, |555\rangle, |656\rangle\}$ , respectively for  $N = L \in \{11, 13, 15, 17\}$ . Density plots in (a) show the evolution of on-site density expectation values,  $\langle n_j(\tau) \rangle$ , with tunneling time  $\tau$  for  $N = 17$  and the four values of  $\eta$  indicated [also marked by arrowheads in panel (c)], and are topped by the spatial density profiles at the final evolution time  $\tau_f = 200$ . The time-averaged value of the density profile width (equation (23)),  $\bar{\sigma}$ , and of the density mean square deviation,  $\bar{F}$  (equation (24), scaled by  $F_0 \equiv F(\tau = 0)$ ), in the interval  $\tau \in [100, 200]$  are shown for varying system size (color coded) as functions of  $\gamma$  in panel (b) and of  $\eta$  in panel (c). The vertical dotted line in (c) marks the threshold value  $\eta_s^c = 1/12$  from equation (21) for  $N \rightarrow \infty$ .

we identify a parametric range  $0.5 \lesssim \gamma \lesssim 10$  where  $\bar{F}$  goes to zero as the width  $\bar{\sigma}$  approaches unity, which is common for all system sizes, correlates unambiguously with the extension of the chaotic phase as inferred from the spectral analysis (cf figures 1(c) and 2(b)), and its appearance is well captured by the analytical estimation from equation (20),  $\gamma_s^c = 1/2$  ( $N \rightarrow \infty$ ). It is worth mentioning that the  $\gamma$ -dependence of the temporal fluctuations of  $\sigma(\tau)$  and  $F(\tau)$  (not shown) also reveals the chaotic phase (as can be anticipated from figure 5).

Hence, the emergence of the dynamical ergodic regime for the staggered states  $|\psi_s\rangle$  is indeed controlled by  $\gamma$ , in accordance with the energy scaling analysis of section 4.

### 5.3. Localized initial density

Lastly, we consider the common experimental situation in which the bosonic density is initially contained in a restricted region of the system whence it expands in time [80]. We mimic this case by taking initial Fock states  $|\psi_\ell\rangle$  at unit density with only  $\ell = 3$  central sites populated.

The time evolution of the density distribution for  $N = 17$  and four values of the scaled tunneling strength  $\eta$  (equation (13)) can be observed in figure 7(a). Like for the staggered configurations, strong interaction ( $\eta = 0.01$ ) entails non-ergodic behavior and persistence of the initial conditions in time. As the tunneling strength grows ( $\eta = 0.043$ ), the cloud starts registering an expansion in time, which has been drastically accelerated at  $\eta = 0.33$ , for which full steady-state homogenization emerges after  $\approx 30$  tunneling times. Upon approaching the weakly interacting limit ( $\eta = 5.88$ ), the

evolution of the density profile displays a characteristic and recurrent interference pattern in time.

These different behaviors are captured by the time-averaged values of the width  $\sigma(\tau)$  and of the spatial density fluctuations  $F(\tau)$ , shown as functions of  $\gamma$  in panel (b), and of  $\eta$  in panel (c). Importantly, the distinct  $\gamma$ -regime of vanishing  $\bar{F}$  and maximal width that one may associate with the chaotic phase witnesses a systematic shift toward larger values for increasing system size. In terms of  $\eta$ , however, the shift is offset, and the behavior of  $\bar{F}$  falls onto a common trend for all  $N$  (up to, arguably, minor finite size effects). From figure 7(c), the ensuing dynamical ergodic regime  $0.08 \lesssim \eta \lesssim 1$  positively correlates with the chaotic phase identified in our spectral analysis (cf figure 2(d)), confirming the validity of the analytical estimation of the threshold value from equation (21),  $\eta_\ell^c = 1/12$  ( $N \rightarrow \infty$ ).

Therefore, the dynamics of initially localized bosonic clouds of fixed size and different particle number, or similar particle number but different size, for the same bare interaction strength, are not comparable. The potential emergence or absence of ergodicity in these cases is controlled by the rescaled tunneling strength  $\eta$ , as concluded from the spectral analysis in the previous section, and here confirmed.

## 6. Conclusions

We have established, in the paradigmatic Bose–Hubbard model, the perfect correspondence between the chaotic region identified from the spectral structure and the emergence of

ergodic dynamics, if only the experimentalist is aware of the trajectory navigated along, across the parametrically evolving energy level structure, as seeded by the specific choice of the many-body initial state of a typical quench experiment. The scaling of the energy expectation value with the number of bosons at fixed particle density permits to conclude whether a Fock initial state witnesses a chaotic phase controlled by the bare tunneling strength  $\gamma = J/U$ , or whether the persistence of chaos in the TL is determined by the parameter  $\eta = J/UN$ , scaled by the number of particles  $N$ . For the assessment of dynamical ergodic behavior in the context of experimental studies with expanding atomic clouds, this, in particular, implies that runs for different initial cloud sizes with similar  $N$ , for the same interaction strength (and hence identical values of  $\gamma$ ), are not comparable: As the onset of chaos is governed by  $\eta$  and not  $\gamma$  for these initial states, the  $\gamma$ -thresholds of chaotic behavior are different for each cloud. Furthermore, we have seen that the onset of chaos for any Fock initial state can be analytically estimated from the excess energy density above the ground state, together with the crossover behavior thereof from the strongly interacting to the non-interacting limit.

### Data availability statement

The data cannot be made publicly available upon publication because they are not available in a format that is sufficiently accessible or reusable by other researchers. The data that support the findings of this study are available upon reasonable request from the authors.

### Acknowledgments

A R thanks Marcos Rigol for helpful discussions. The authors acknowledge support by the state of Baden-Württemberg through bwHPC and the German Research Foundation (DFG) through Grants No. INST 40/467-1 FUGG (JUSTUS cluster), No. INST 40/575-1 FUGG (JUSTUS 2 cluster), and No. 402552777, and by Ministerio de Ciencia e Innovación/Agencia Estatal de Investigación (Spain) through Grant No. PID2020-114830GB-I00. E.G.C. acknowledges support from the Georg H Endress foundation. This project (EOS 40007526) has received funding from the FWO and F.R.S-FNRS under the Excellence of Science (EOS) programme. This research has made use of the high performance computing resources of the Castilla y León Supercomputing Center (SCAYLE, [www.scayle.es](http://www.scayle.es)), financed by the European Regional Development Fund (ERDF), and of the CSUC (Consorci de Serveis Universitaris de Catalunya) supercomputing resources. We thankfully acknowledge RES resources provided by the Galician Supercomputing Center (CESGA) in FinisTerra III to activity FI-2024-2-0027. The supercomputer FinisTerra III and its permanent data storage system have been funded by the Spanish Ministry of Science and Innovation, the Galician Government and the European Regional Development Fund (ERDF).

### Appendix A. Energy expectation value for maximally mixed state

Since the diagonal of Hamiltonian (1) is solely determined by the interaction term, the energy expectation value for the maximally mixed state  $\rho_{\text{MM}} = \mathbb{1}/\mathcal{D}(N, L)$ , where we recall that  $\mathcal{D}(N, L) = \binom{N+L-1}{N}$ , can be evaluated straightforwardly,

$$\begin{aligned} \text{Tr}(H\rho_{\text{MM}}) &= \frac{1}{\mathcal{D}(N, L)} \frac{U}{2} \text{Tr} \left[ \sum_{j=1}^L \hat{n}_j (\hat{n}_j - 1) \right] \\ &= \frac{U}{2} \left( \frac{1}{\mathcal{D}(N, L)} \sum_{j=1}^L \text{Tr} \hat{n}_j^2 - N \right) \\ &= \frac{U}{2} \left( \frac{L}{\mathcal{D}(N, L)} \sum_{\|n\|_1=N} n_1^2 - N \right) \\ &= \frac{U}{2} \left( L \sum_{k=1}^N k^2 \frac{\mathcal{D}(N-k, L-1)}{\mathcal{D}(N, L)} - N \right) \\ &= U \frac{N(N-1)}{L+1}. \end{aligned} \quad (\text{A1})$$

For the case of constant bosonic density,  $n = N/L$ ,

$$\text{Tr}(H\rho_{\text{MM}}) = U [nN - n(n+1) + O(N^{-1})], \quad (\text{A2})$$

i.e. the energy expectation value scales linearly with particle number,  $\text{Tr}(H\rho_{\text{MM}}) \simeq UnN$ , as the thermodynamic limit is approached.

### Appendix B. Chebyshev expansion technique for time evolution

The time evolution of a generic initial state  $|\psi_0\rangle$ , induced by the time-independent Bose–Hubbard Hamiltonian, can be numerically implemented by expanding the corresponding time evolution operator  $\mathcal{U}(\tau) = e^{-i(H/J)\tau}$ , with  $\tau \equiv Jt/\hbar$ , in terms of Chebyshev polynomials of the first kind  $T_n(x)$ ,  $n \geq 0$  [81]. A rescaled Hamiltonian  $\tilde{H}$  must be defined from  $H/J = a\tilde{H} + b\mathbb{1}$ , with

$$a = (E_{\text{max}} - E_{\text{min}})/2J, \quad b = (E_{\text{max}} + E_{\text{min}})/2J, \quad (\text{B1})$$

to ensure that  $\text{Spec}(\tilde{H}) \in [-1, 1]$ . The forward evolution from time  $\tau$  to  $\tau + \Delta\tau$  can then be written as

$$\mathcal{U}(\Delta\tau) |\psi(\tau)\rangle \simeq e^{-ib\Delta\tau} \left[ c_0 |v_0(\tau)\rangle + 2 \sum_{n=1}^M c_n |v_n(\tau)\rangle \right], \quad (\text{B2})$$

where the coefficients are determined by Bessel functions,  $J_n(x)$ ,

$$c_n \equiv (-i)^n J_n(a\Delta\tau), \quad (\text{B3})$$

and  $M$  denotes the chosen cut-off for the expansion. The vector states in the series follow from the recursion relation of the Chebyshev polynomials,

$$|v_0(\tau)\rangle \equiv |\psi(\tau)\rangle, \quad (\text{B4a})$$

$$|v_1(\tau)\rangle \equiv T_1(\tilde{H})|v_0(\tau)\rangle = \tilde{H}|\psi(\tau)\rangle, \quad (\text{B4b})$$

$$|v_{n+1}(\tau)\rangle \equiv T_{n+1}(\tilde{H})|v_0(\tau)\rangle = 2\tilde{H}|v_n(\tau)\rangle - |v_{n-1}(\tau)\rangle. \quad (\text{B4c})$$

Given a value of  $a\Delta\tau$ , the coefficients  $c_n$  decay faster than exponentially with  $n$  for large  $n$ , and hence an accurate expansion may be achieved with a reasonable number of terms, although, for a targeted precision, the number of terms will increase for larger spectral width  $a$  and/or chosen time step  $\Delta\tau$ . The implementation of (B2), as can be seen in equations (B4), only requires matrix-vector multiplications, which can be efficiently parallelized [82–85].

We carry out dynamics without imposing any truncation of the maximum occupation number in the Fock basis, and always take initial Fock states that exhibit parity symmetry to reduce the dynamically available Hilbert space. We consider systems at unit density up to  $L = 17$  with Hilbert subspace  $\mathcal{H}^+$  of size  $\mathcal{D}^+ \simeq 5.8 \times 10^8$ . The expansion cut-off  $M$  is chosen to keep all terms with coefficients obeying  $|c_n| \geq 10^{-12}$  for any  $\gamma = J/U$ . In all cases, we have checked that the chosen precision is enough to ensure convergence of the calculated observables.

## ORCID iDs

Lukas Pausch  <https://orcid.org/0000-0002-9859-6660>  
 Edoardo G Carnio  <https://orcid.org/0000-0002-1270-7607>  
 Alberto Rodríguez  <https://orcid.org/0000-0002-3102-8781>

## References

- [1] Hittmair O 1972 *Lehrbuch der Quantentheorie* (Verlag Karl Thieme)
- [2] Geisel T, Radons G and Rubner J 1986 Kolmogorov-Arnol'd-Moser barriers in the quantum dynamics of chaotic systems *Phys. Rev. Lett.* **57** 2883
- [3] Du M L and Delos J B 1987 Effect of closed classical orbits on quantum spectra: Ionization of atoms in a magnetic field *Phys. Rev. Lett.* **58** 1731
- [4] Brunner E, Pausch L, Carnio E G, Dufour G, Rodríguez A and Buchleitner A 2023 Many-Body Interference at the Onset of Chaos *Phys. Rev. Lett.* **130** 080401
- [5] 1989 Chaos and Quantum Physics *École d'été de Physique théorique des Houches, Session LII*, ed M-J Giannoni, A Voros and J Zinn-Justin (North Holland)
- [6] Buchleitner A and Delande D 1993 Quantum dynamics of a circular rydberg state in a microwave field *Phys. Rev. Lett.* **71** 3633
- [7] Carvalho A R R and Buchleitner A 2004 Web-assisted tunneling in the kicked harmonic oscillator *Phys. Rev. Lett.* **93** 204101
- [8] Brünner T, Dufour G, Rodríguez A and Buchleitner A 2018 Signatures of indistinguishability in Bosonic Many-Body Dynamics *Phys. Rev. Lett.* **120** 210401
- [9] Evrard B, Pizzi A, Mistakidis S I and Dag C B 2024 Quantum many-body scars from unstable periodic orbits *Phys. Rev. B* **110** 144302
- [10] Berry M V 1977 Regular and irregular semiclassical wavefunctions *J. Phys. A: Gen. Phys.* **10** 2083
- [11] Tanner G, Richter K and Rost J-M 2000 The theory of two-electron atoms: between ground state and complete fragmentation *Rev. Mod. Phys.* **72** 497
- [12] Gutzwiller M C 1990 *Chaos in Classical and Quantum Mechanics* (Springer)
- [13] Laskar J 1993 Frequency analysis for multi-dimensional systems. global dynamics and diffusion *Physica D* **67** 257
- [14] von Milczewski J, Diercksen G H F and Uzer T 1996 Computation of the arnol'd web for the hydrogen atom in crossed electric and magnetic fields *Phys. Rev. Lett.* **76** 2890
- [15] Schlagheck P and Buchleitner A 1999 Stable classical configurations in strongly driven helium *Physica D* **131** 110
- [16] Stöber J, Bäcker A and Ketzmerick R 2024 Quantum transport through partial barriers in higher-dimensional systems *Phys. Rev. Lett.* **132** 047201
- [17] Jaksch D, Bruder C, Cirac J I, Gardiner C W and Zoller P 1998 Cold bosonic atoms in optical lattices *Phys. Rev. Lett.* **81** 3108
- [18] Trimborn F, Witthaut D and Korsch H J 2009 Beyond mean-field dynamics of small Bose-Hubbard systems based on the number-conserving phase-space approach *Phys. Rev. A* **79** 013608
- [19] Buchleitner A and Kolovsky A R 2003 Interaction-induced decoherence of atomic bloch oscillations *Phys. Rev. Lett.* **91** 253002
- [20] Kolovsky A R and Buchleitner A 2004 Quantum chaos in the Bose-Hubbard model *Europhys. Lett.* **68** 632
- [21] Ponomarev A V, Madro nero J, Kolovsky A R and Buchleitner A 2006 Atomic current across an optical lattice *Phys. Rev. Lett.* **96** 050404
- [22] Biroli G, Kollath C and Läuchli A M 2010 Effect of rare fluctuations on the thermalization of isolated quantum systems *Phys. Rev. Lett.* **105** 250401
- [23] Kollath C, Roux G, Biroli G and Läuchli A M 2010 Statistical properties of the spectrum of the extended Bose-Hubbard model *J. Stat. Mech. Theory Exp.* **2010** 08011
- [24] Beugeling W, Moessner R and Haque M 2014 Finite-size scaling of eigenstate thermalization *Phys. Rev. E* **89** 042112
- [25] Beugeling W, Moessner R and Haque M 2015 Off-diagonal matrix elements of local operators in many-body quantum systems *Phys. Rev. E* **91** 012144
- [26] Beugeling W, Andreanov A and Haque M 2015 Global characteristics of all eigenstates of local many-body Hamiltonians: participation ratio and entanglement entropy *J. Stat. Mech. Theory Exp.* **2015** 02002
- [27] Dubertrand R and Müller S 2016 Spectral statistics of chaotic many-body systems *New J. Phys.* **18** 033009
- [28] Beugeling W, Bäcker A, Moessner R and Haque M 2018 Statistical properties of eigenstate amplitudes in complex quantum systems *Phys. Rev. E* **98** 022204
- [29] de la Cruz J, Lerma-Hernández S and Hirsch J G 2020 Quantum chaos in a system with high degree of symmetries *Phys. Rev. E* **102** 032208
- [30] Russomanno A, Fava M and Fazio R 2020 Nonergodic behavior of the clean Bose-Hubbard chain *Phys. Rev. B* **102** 144302
- [31] Pausch L, Carnio E G, Rodríguez A and Buchleitner A 2021 Chaos and ergodicity across the energy spectrum of interacting bosons *Phys. Rev. Lett.* **126** 150601



- [32] Pausch L, Carnio E G, Buchleitner A and Rodríguez A 2021 Chaos in the Bose-Hubbard model and random two-body Hamiltonians *New J. Phys.* **23** 123036
- [33] Pausch L, Buchleitner A, Carnio E G and Rodríguez A 2022 Optimal route to quantum chaos in the Bose-Hubbard model *J. Phys. A* **55** 324002
- [34] Kollath C, Läuchli A M and Altman E 2007 Quench dynamics and nonequilibrium phase diagram of the Bose-Hubbard model *Phys. Rev. Lett.* **98** 180601
- [35] Läuchli A M and Kollath C 2008 Spreading of correlations and entanglement after a quench in the one-dimensional Bose-Hubbard model *J. Stat. Mech. Theory Exp.* **2008** 05018
- [36] Cramer M, Flesch A, McCulloch I P, Schollwöck U and Eisert J 2008 Exploring local quantum many-body relaxation by atoms in optical superlattices *Phys. Rev. Lett.* **101** 063001
- [37] Roux G 2009 Quenches in quantum many-body systems: one-dimensional Bose-Hubbard model reexamined *Phys. Rev. A* **79** 021608(R)
- [38] Roux G 2010 Finite-size effects in global quantum quenches: examples from free bosons in an harmonic trap and the one-dimensional Bose-Hubbard model *Phys. Rev. A* **81** 053604
- [39] Barmettler P, Poletti D, Cheneau M and Kollath C 2012 Propagation front of correlations in an interacting Bose gas *Phys. Rev. A* **85** 053625
- [40] Vidmar L, Langer S, McCulloch I P, Schneider U, Schollwöck U and Heidrich-Meisner F 2013 Sudden expansion of Mott insulators in one dimension *Phys. Rev. B* **88** 235117
- [41] Meinert F, Mark M J, Kirilov E, Lauber K, Weinmann P, Gröbner M and Nägerl H-C 2014 Interaction-Induced quantum phase revivals and evidence for the transition to the quantum chaotic regime in 1D atomic Bloch oscillations *Phys. Rev. Lett.* **112** 193003
- [42] Sorg S, Vidmar L, Pollet L and Heidrich-Meisner F 2014 Relaxation and thermalization in the one-dimensional Bose-Hubbard model: a case study for the interaction quantum quench from the atomic limit *Phys. Rev. A* **90** 033606
- [43] Andraschko F and Sirker J 2015 Propagation of a single-hole defect in the one-dimensional Bose-Hubbard model *Phys. Rev. B* **91** 235132
- [44] Despres J, Villa L and Sanchez-Palencia L 2019 Twofold correlation spreading in a strongly correlated lattice Bose gas *Sci. Rep.* **9** 4135
- [45] Wittmann W. K., Castro E R, Foerster A and Santos L F 2022 Interacting bosons in a triple well: preface of many-body quantum chaos *Phys. Rev. E* **105** 034204
- [46] Berke C, Varvelis E, Trebst S, Altland A and DiVincenzo D P 2022 Transmon platform for quantum computing challenged by chaotic fluctuations *Nat. Commun.* **13** 2495
- [47] Basilewitsch D, Börner S-D, Berke C, Altland A, Trebst S and Koch C P 2023 Chaotic fluctuations in a universal set of transmon qubit gates (arXiv:2311.14592)
- [48] Börner S-D, Berke C, DiVincenzo D P, Trebst S and Altland A 2024 Classical chaos in quantum computers *Phys. Rev. Res.* **6** 033128
- [49] Choi J *et al* 2023 Preparing random states and benchmarking with many-body quantum chaos *Nature* **613** 468
- [50] Mark D K, Choi J, Shaw A L, Endres M and Choi S 2023 Benchmarking quantum simulators using ergodic quantum dynamics *Phys. Rev. Lett.* **131** 110601
- [51] Lewenstein M, Sanpera A, Ahufinger V, Damski B, Sen A and Sen U 2007 Ultracold atomic gases in optical lattices: mimicking condensed matter physics and beyond *Adv. Phys.* **56** 243
- [52] Bloch I, Dalibard J and Zwerger W 2008 Many-body physics with ultracold gases *Rev. Mod. Phys.* **80** 885
- [53] Cazalilla M A, Citro R, Giamarchi T, Orignac E and Rigol M 2011 One dimensional bosons: from condensed matter systems to ultracold gases *Rev. Mod. Phys.* **83** 1405
- [54] Krutitsky K V 2016 Ultracold bosons with short-range interaction in regular optical lattices *Phys. Rep.* **607** 1
- [55] Pausch L 2022 Eigenstate structure and quantum chaos in the Bose-Hubbard Hamiltonian *Dissertation* Albert-Ludwigs-Universität Freiburg (<https://doi.org/10.6094/UNIFR/228554>)
- [56] Cheneau M, Barmettler P, Poletti D, Endres M, Schauf P, Fukuhara T, Gross C, Bloch I, Kollath C and Kuhr S 2012 Light-cone-like spreading of correlations in a quantum many-body system *Nature* **481** 484
- [57] Meinert F, Mark M J, Kirilov E, Lauber K, Weinmann P, Gröbner M, Daley A J and Nägerl H-C 2014 Observation of many-body dynamics in long-range tunneling after a quantum quench *Science* **344** 1259
- [58] Kaufman A M, Tai M E, Lukin A, Rispoli M, Schittko R, Preiss P M and Greiner M 2016 Quantum thermalization through entanglement in an isolated many-body system *Science* **353** 794
- [59] Rispoli M, Lukin A, Schittko R, Kim S, Tai M E, Léonard J and Greiner M 2019 Quantum critical behaviour at the many-body localization transition *Nature* **573** 385
- [60] Lukin A, Rispoli M, Schittko R, Tai M E, Kaufman A M, Choi S, Khemani V, Léonard J and Greiner M 2019 Probing entanglement in a many-body-localized system *Science* **364** 256
- [61] Bohrdt A, Kim S, Lukin A, Rispoli M, Schittko R, Knap M, Greiner M and Léonard J 2021 Analyzing nonequilibrium quantum states through snapshots with artificial neural networks *Phys. Rev. Lett.* **127** 150504
- [62] Takasu Y, Yagami T, Asaka H, Fukushima Y, Nagao K, Goto S, Danshita I and Takahashi Y 2020 Energy redistribution and spatiotemporal evolution of correlations after a sudden quench of the Bose-Hubbard model *Sci. Adv.* **6** eaba9255
- [63] Léonard J, Kim S, Rispoli M, Lukin A, Schittko R, Kwan J, Demler E, Sels D and Greiner M 2023 Probing the onset of quantum avalanches in a many-body localized system *Nat. Phys.* **19** 481
- [64] Trotzky S, Chen Y A, Flesch A, McCulloch I P, Schollwöck U, Eisert J and Bloch I 2012 Probing the relaxation towards equilibrium in an isolated strongly correlated one-dimensional Bose gas *Nat. Phys.* **8** 325
- [65] Bordia P, Lüschen H P, Hodgman S S, Schreiber M, Bloch I and Schneider U 2016 Coupling identical one-dimensional many-body localized systems *Phys. Rev. Lett.* **116** 140401
- [66] Rubio-Abadal A, Choi J-Y, Zeiher J, Hollerith S, Rui J, Bloch I and Gross C 2019 Many-Body delocalization in the presence of a quantum bath *Phys. Rev. X* **9** 041014
- [67] Ronzheimer J P, Schreiber M, Braun S, Hodgman S S, Langer S, McCulloch I P, Heidrich-Meisner F, Bloch I and Schneider U 2013 Expansion dynamics of interacting bosons in homogeneous lattices in one and two dimensions *Phys. Rev. Lett.* **110** 205301
- [68] Choi J-Y, Hild S, Zeiher J, Schauf P, Rubio-Abadal A, Yefsah T, Khemani V, Huse D A, Bloch I and Gross C 2016 Exploring the many-body localization transition in two dimensions *Science* **352** 1547
- [69] Lindinger J, Buchleitner A and Rodríguez A 2019 Many-Body multifractality throughout bosonic superfluid and mott insulator phases *Phys. Rev. Lett.* **122** 106603
- [70] Note that this staggered state is not uniquely defined, since the sites may be sorted into any order without changing the energy. However, as they all have the same energy and similar energy widths, they will exhibit qualitatively the same dynamical behavior.

- [71] This is due to the fact that the mean energy of any Fock state depends only on the interaction term. Thus, as  $\gamma \rightarrow \infty$ , the corresponding  $\varepsilon$  is entirely defined by the spectral bounds  $E_{\max} = -E_{\min} = 2NJ$ , yielding  $\varepsilon \rightarrow 0.5$ .
- [72] Haake F, Gnutzmann S and Kuś M 2018 *Quantum Signatures of Chaos (Springer Series in Synergetics)* ed H Haken (Springer) (<https://doi.org/10.1007/978-3-319-97580-1>)
- [73] It must be noted, though, that the thermodynamic limit here under closer inspection is *distinct* from the semiclassical limit which is at the very core of quantum chaos, inasmuch as, in the latter limit, characteristic quantum features are compared to a well-defined underlying classical phase space structure. Since the density is fixed in the thermodynamic limit, and the particle number  $N$  is increased, so has to increase the lattice's length  $L$ , and thus the number of degrees of freedom, which, in turn, controls the dimension of phase space. Taking the thermodynamic limit we thus simultaneously send the phase space dimension to infinity.
- [74] Castro E R, W. K W, Chávez-Carlos J, Roditi I, Foerster A and Hirsch J G 2024 Quantum-classical correspondence in a triple-well bosonic model: from integrability to chaos *Phys. Rev. A* **109** 032225
- [75] Hiller M, Kottos T and Geisel T 2006 Complexity in parametric Bose-Hubbard Hamiltonians and structural analysis of eigenstates *Phys. Rev. A* **73** 061604(R)
- [76] Hiller M, Kottos T and Geisel T 2009 Wave-packet dynamics in energy space of a chaotic trimeric Bose-Hubbard system *Phys. Rev. A* **79** 023621
- [77] Note that the oscillations observable on transient time scales before equilibration can be attributed to particles being reflected at the edge sites: such oscillations are prominently seen in the chaotic  $\gamma$ -range, and the their frequency is found to decrease as the lattice, and hence the time to travel from one edge to another, becomes larger.
- [78] Srednicki M 1996 Thermal fluctuations in quantized chaotic systems *J. Phys. A: Math. Gen.* **29** L75
- [79] Srednicki M 1999 The approach to thermal equilibrium in quantized chaotic systems *J. Phys. A: Math. Gen.* **32** 1163
- [80] Venzl H, Daley A J, Mintert F and Buchleitner A 2009 Statistics of Schmidt coefficients and the simulability of complex quantum systems *Phys. Rev. E* **79** 056223
- [81] Weiße A and Fehske H 2008 Chebyshev expansion techniques *Computational Many-Particle Physics* (Springer) pp 545–77
- [82] Balay S et al 2023 PETSc/TAO Users Manual *Technical Report ANL-21/39 - Revision 3.20* Argonne National Laboratory (<https://doi.org/10.2172/2205494>)
- [83] Balay S, Gropp W D, McInnes L C and Smith B F 1997 Efficient management of parallelism in object oriented numerical software libraries *Modern Software Tools in Scientific Computing* ed E Arge, A M Bruaset and H P Langtangen (Birkhäuser Press) pp 163–202
- [84] Balay S et al 2023 *Petsc Web Page* (available at: <https://petsc.org/>)
- [85] Hernandez V, Roman J E and Vidal V 2005 SLEPc: a scalable and flexible toolkit for the solution of eigenvalue problems *ACM Trans. Math. Softw.* **31** 351